

Steady inertial flow of a compressible fluid in a spatially periodic channel under large pressure drops: a multiscale semi-analytical approach

Valentina Biagioni^a, Bram Huygens^b, Giuseppe Procopio^a, Maria Anna Murmura^a, Gert Desmet^b, Stefano Cerbelli^{a,*}

^a*Dipartimento di Ingegneria Chimica - Sapienza Università di Roma , Via Eudossiana 18, Roma, 00184, , Italy*
^b*Dept. of Chemical Engineering - Vrije Universiteit Brussel, Bd de la Plaine 2, 1050 Ixelles, Brussel, 1050 Ixelles, , Belgium*

Abstract

Spatially-periodic channels are increasingly attracting attention as an efficient alternative to packed columns for a number of analytical and engineering processes. In incompressible flows, the periodic geometry allows to compute the flow structure by solving the Navier-Stokes (NS) equations in the minimal periodic cell of the structure, however large the pressure gradient. Besides, when gas flow under large pressure drops are dealt with, the velocity field is not periodic because of the density dependence on pressure. In this case, the momentum balance equations must be solved numerically on the entire channel, thereby requiring massive computational effort. Based on the marked separation of scales between the length of the periodic cell and the overall channel length characterizing many applications we develop a general method for predicting both the large-scale pressure and velocity profiles, and the small-scale flow structure. The approach proposed is based on the assumption that the local dimensionless pressure drop as a function of the Reynolds number, say $g(\text{Re})$, can be estimated from the solution of the incompressible NS equations within the minimal periodic cell of the channel. From the knowledge of $g(\text{Re})$, the pressure profile $P(Z)$ vs the large scale axial coordinate Z is derived analytically by quadratures. We show how qualitatively different profiles $P(Z)$ can be obtained depending on the equation of state the gas. The approach is validated by comparing the predicted profiles with the full-scale numerical solution of the compressible NS equations in different axially-symmetric periodic channel geometries.

1. Introduction

Microchannels are attracting increasing interest in numerous analytical and engineering fields, including chemical reactors [1–4], heat transfer devices [5, 6], and chromatography [7], due to their capability of enhancing heat and mass transfer rates while avoiding the presence of moving mechanical components. An accurate description of these devices requires the solution of mass, heat, and momentum balance equations. With regards to momentum, issues may arise in the description of flow structure due to the significant pressure gradients that often arise. Clearly,

*

Email address: stefano.cerbelli@uniroma1.it (Stefano Cerbelli)

this issue is not relevant in the case of incompressible fluids; however, it becomes important when compressibility cannot be neglected.

The need to accurately describe the flow of compressible fluids has been familiar for some time. A consistent body of work has been developed for rarified gas conditions, due to the important implications as regards momentum, mass and energy transport in ordered and disordered media whose pores are characterized by a wide distribution of lengthscales (see, e.g., [8–11]). In this context, the gaseous nature of the fluid mainly impacts upon the structure of the velocity profile at the solid surfaces confining the flow, thereby determining a variety of fluid dynamic regimes, from continuum, to slip, transitional, and, ultimately, free-molecular flow, as the Knudsen number increases from order 10^{-2} to unity and beyond.

A comparatively smaller number of studies focused on relatively high pressure conditions to unveil the effect of the coupling between density and pressure on the flow structure in empty channels. For instance, Proud’homme et al. [12] developed a two-dimensional solution for the velocity and pressure profiles in steady, laminar, isothermal flow of an ideal gas in long tubes as a double perturbation expansion in the radius to length ratio of the tube, β , and the relative pressure drop, ϵ . Their results validate the Hagen-Poiseuille assumption of local fluid incompressibility for the obtainement of the pressure profile. Similar approaches were employed by Venerus [13, 14]. An experimental study of the problem was carried out by Celata et al. [15, 16], who determined the friction factor for a gas flow in a microchannel and found an excellent agreement with the Hagen-Poiseuille correlation. The direct numerical solution through Finite Element Method (FEM) approach of gas flow in single empty microchannels [17] and in intercrossing [18] microchannel networks has been also reported. Because of the multiscale nature of the problem, however, in these studies the ratio of the characteristic dimension of the cross-section to the channel length was limited to 10^{-2} . Another aspect that must be considered is the range of Reynolds number for which the flow of a compressible fluid is laminar. This problem was dealt with by Novopashim et al. [19], who studied the effect of the value of the second Virial coefficient on the critical Reynolds number for which there is a transition from laminar to turbulent flow of a gas in a cylindrical channel and found that appreciable differences in the values of the critical Reynolds numbers exist at high pressures. Vocale et al. [20], on the other hand, carried out a numerical study on the effect of fluid compressibility on the friction factor in microchannels having a square cross-section. They found that compressibility leads to an increase in the average friction factor, and that the value of the Reynolds number at which these effects become significant decreases in microchannels with smaller cross-section.

As regards the case of periodic channels, the importance of making available a theoretical and computationally affordable framework for predicting the flow structure can hardly be overestimated. Periodic channel geometries (e.g. obtained using Triply Periodic Minimal Surfaces as solid fillers embedded in the channel [21–24]) exploited in microturbine cooling, or micropillar array columns used for gas chromatography [25, 26] provide just two out of many examples that could greatly benefit from an accurate description of the small-scale and large-scale structure of the compressible flow. In these examples, the detailed knowledge of the small- and large-scale structure of the flow could be exploited for enforcing simplifying assumptions in the mass and energy transport equations, thus allowing to interpret experimental results of existing prototypes, on the one hand, and/or to define optimal shapes for enhancing the heat transfer coefficient in micro heat exchangers, or lowering the axial dispersion coefficient in gas chromatography.

More generally, the periodic geometry template could serve as a an idealized model of random packing [27–29], thus enlarging the domain of application of the approach proposed to classical

chemical engineering equipment such as adsorption columns and fixed bed gas-solid or catalytic reactors. In this perspective, the assessment of the fluid dynamics features of the gas flow under large pressure drops in periodic media constitutes the preliminary yet fundamental piece of information allowing to define a new class of problems in Brenner’s theory of macrotransport processes in periodic media [30], where the effective transport coefficients resulting from the intertwined action of molecular diffusion and convection at the scale of single cell of the periodic structure are not constant throughout the medium even in the isothermal case because of their dependence on the large-scale pressure profile.

The above observations highlight both the importance of understanding and accurately describing the flow of compressible fluids in periodic channels and the potential opportunities of employing these devices for heat and mass transfer operations. Specifically, it is foreseeable that the detailed knowledge of the large- and small-scale structure of the velocity field in the compressible case will make it possible to devise geometries and operating conditions tailored to control mixing, dispersion and heat transport in gas flows. This would allow to trace over the results obtained for microchannels processing liquid solutions, where the strictly spatially periodic structure of the flow has been exploited for investigating the relationship between flow structure and residence time distribution[31, 32], and enhancing the performance of micromixers, microreactors[33–36] and microfluidics-assisted separation columns for liquid chromatography [37, 38].

To the best of these authors’ knowledge, however, a computationally affordable method for describing the flow of compressible fluids in such channels has never been proposed. In the present work, we attempt to fill this gap by developing a method for predicting the large-scale pressure and velocity profiles downstream a periodic channel, as well as the small-scale flow structure, taking advantage of the simplifying assumptions made possible by the significant separation of scales between the single periodic cell and the overall channel length that characterize typical applications. We show that an accurate description of the flow is made possible by a multiscale approach, where the gas velocity is split into a large-scale piecewise-constant factor and a strictly periodic incompressible component. The approach proposed hinges on the observations that, notwithstanding the considerable large variations of density, velocity and pressure that may arise (depending on the geometry) downstream the channel axis, mass conservation implies that at steady-state conditions the cross-sectional average of the product between the density and the axial velocity component is constant along the channel axis. On the assumption that the viscosity variations can be neglected, this allows to define a Reynolds number characterizing the entire flow, and to effectively decouple the dependence of the variables on the the large- and the small-scale coordinates.

The article is organized as follows. In Section 2, we describe the problem being dealt with and illustrate the channel geometries considered as case studies along with the definition of the coordinate systems adopted. In Section 3 the theoretical approach adopted is discussed. The results are presented in Section 4 and discussed in Section 5, together with a perspective towards possible generalizations of the approach to non-isothermal flows and/or random media.

2. Statement of the problem

We consider the pressure-driven, compressible flow of a gas through an axially periodic channel. Figure 1 depicts an example of periodic channels, together with the global and local (or cell) coordinate systems.

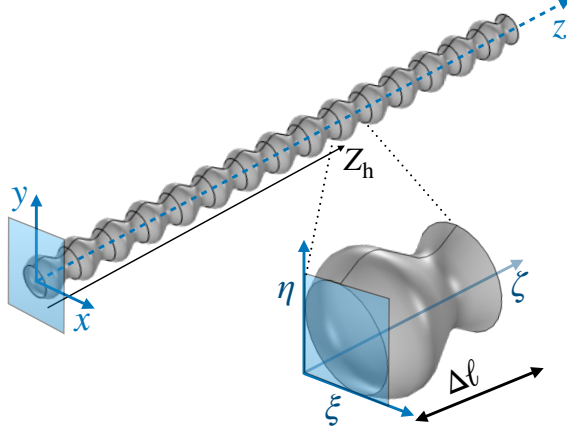


Figure 1: Schematic representation of the periodic channel geometry and of the global and local coordinate systems, x, y, z and ξ, η, ζ , respectively.

In what follows, the spatial period of the geometry, say $\Delta\ell$, is assumed to be orders of magnitude smaller than the overall length, L , of the channel, i.e. $\Delta\ell/L \ll 1$. Also, the flow is assumed Newtonian, steady, non-turbulent, and isothermal (see Section 5.1 for more details on this assumption). In the incompressible case, the velocity field can be obtained through the solution of Navier-Stokes equations on the minimal periodic cell of the structure, thereby assuming that, beyond a short spatial transient, the flow is periodic over the same length $\Delta\ell$ defining the geometry of the system. In the case of compressible fluids, however, the velocity field cannot be expected in general to be periodic. This is because the existence of a pressure drop along the channel axis causes the simultaneous variation of the fluid density and (by mass conservation) of the average axial velocity. The flow structure must therefore be obtained by solving the entire channel structure of the compressible Navier-Stokes Boundary Value Problem,

$$\rho \mathbf{v} \cdot \nabla \mathbf{v} = \mu \nabla^2 \mathbf{v} + \frac{\mu}{3} \nabla (\nabla \cdot \mathbf{v}) - \nabla p; \quad \nabla \cdot (\rho \mathbf{v}) = 0 \quad (1)$$

equipped with no-slip Boundary Conditions (BCs) onto all the solid surfaces confining the flow, and with assigned pressure values at the inlet and outlet cross-sections of the channel. In Eq. (1), $\rho(x, y, z)$, $\mathbf{v}(x, y, z)$, $p(x, y, z)$ represent the local density, velocity and pressure of the gas. The constant density constraint of the incompressible case is here replaced by the Equation Of State (EOS), $f(\rho, p, T) = 0$, that characterizes the volumetric behavior of the gas. In the case of widely separated scales, where $\Delta\ell/L$ is of order 10^{-3} or below, the direct numerical approach to Eq. (1) may result troublesome. This is especially true in inherently three-dimensional flows in the inertial regime because of the possible onset of thin boundary layers, which, even at the scale of the single periodic module, require a large number of degrees of freedom to be captured. Thus, for channels embedding a large number of cells (e.g. order $10^3 \div 10^5$), the computational effort becomes massive, making it impractical to obtain accurate numerical solutions of the flow when geometries of practical interest are to be dealt with.

2.1. Case studies

As case studies, the three geometries depicted in Fig. 2 are next considered.

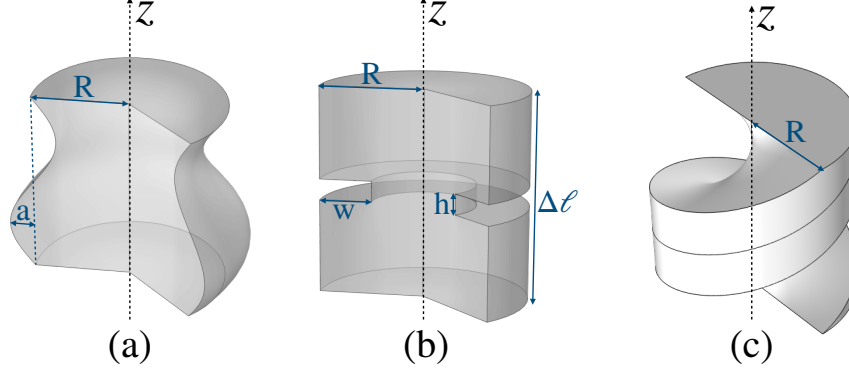


Figure 2: Elementary cells of the periodic channel geometries considered as case studies.

The channel shapes depicted in panels (a) and (b) of the figure are axial-symmetric and will be used to compare and contrast the predictions stemming from the approach proposed in this article with the full solution of the Navier-Stokes problem expressed by Eq. (1) for the compressible isothermal flow of an ideal gas. In all of the cases represented, the aspect ratio of the periodic cell has been chosen so that $\Delta \ell = 2R$. The wall of the sinusoidal channel of Fig. 2-(a) is specified by the equation

$$\sqrt{\tilde{x}^2 + \tilde{y}^2} = \tilde{R} + \tilde{a} \sin(2\pi \tilde{z}) \quad (2)$$

where $\tilde{x} = x/\Delta \ell$, $\tilde{y} = y/\Delta \ell$ and $\tilde{z} = z/\Delta \ell$ are nondimensional coordinates scaled to the length of the periodic cell, and where the parameters $\tilde{R} = R/\Delta \ell$ and $\tilde{a} = a/\Delta \ell$ represent the dimensionless average channel radius and the amplitude of the sinusoidal oscillation, respectively. In the case investigated, the dimensionless amplitude of the sinusoidal profile has been fixed equal to $\tilde{a} = 0.125$. As regards the baffled channel (panel b), the depth, w , and thickness, h , of the wall indentation have been chosen so that $w/R = 1/2$ and $h/\Delta \ell = 1/10$. The shape in Fig. 2-(c) is obtained by inserting a helicoidal baffle in a cylindrical channel (for better visualization, only one of the two halves of the structure is depicted in the figure). The helicoidal surface is specified by the parametric equations

$$\begin{cases} \tilde{x} &= u \cos(2\pi v) \\ \tilde{y} &= u \sin(2\pi v) \\ \tilde{z} &= v \end{cases} \quad (3)$$

where $0 \leq u \leq R/\Delta \ell$ (R being the radius of the cylinder) and $0 \leq v \leq L/\Delta \ell$. The helicoidal channel of Fig. 2-c will be taken as a representative example of a three-dimensional periodic flow where the inertial term of momentum balance equation shows a strong influence of the streamline geometry even at relatively low values of the Reynolds number.

3. Theoretical approach and analytical prediction of pressure and velocity large-scale profiles

3.1. Decomposition of the field variables in small- and large-scale components

Tracing over classical approaches of homogenization theory [30, 39], we represent the axial coordinate z as $z = Z_h + \tilde{z}$, where $Z_h = [z/\Delta\ell] \Delta\ell$ (“ $[u]$ ” being the integer part of u) identifies the distance of the h -th cell from the channel inlet (see Fig. 1). The variable $0 \leq \tilde{z} \leq \Delta\ell$ is a local coordinate spanning the axial extent of the cell, i.e. $\tilde{z} = (z - Z_h)$. In the approach next proposed the fluid is supposed locally incompressible, thus implying that $\rho(x, y, z)$ is represented by a piecewise-constant function,

$$\rho(x, y, z) = R(Z_h) \quad (4)$$

undergoing finite jumps when crossing the boundary between two contiguous periodic cells. By enforcing the above structure for the the density field, in the Appendix we show that an approximation to the full-scale solution of the compressible Navier-Stokes problem in the periodic geometry for both velocity and pressure can be expressed in terms of the product of large-scale piecewise-constant functions times a small-scale (dimensionless) field that captures the fluctuations of the field variables at the characteristic length of the cell size.

As regards the velocity, this is represented as

$$\mathbf{v}(x, y, z) = V(Z_h) \mathbf{v}_c(x, y, \tilde{z}) \quad (5)$$

and where $V(Z_h)$ [m/s] represents the cell-averaged value of the large-scale component of the axial velocity,

$$V(Z_h) = \int_{V_c^{(h)}} \mathbf{v} \cdot \mathbf{n}_z \, dx \, dy \, dz / \int_{V_c^{(h)}} dx \, dy \, dz \quad (6)$$

and where $\mathbf{v}_c(x, y, \tilde{z})$ is a dimensionless vector-valued function periodic in the interval $0 \leq \tilde{z} \leq \Delta\ell$. In Eq. (6), $V_c^{(h)}$ denotes the volume of the generic h -th cell downstream the channel and \mathbf{n}_z is a unit vector aligned with the z -axis.

The pressure, $p(x, y, z)$, is also decomposed into a large-scale component, say $P(Z_h) = R(Z_h)V^2(Z_h)$, which is assumed to scale as the density of the kinetic energy, times a small-scale dimensionless pressure field, as

$$p(x, y, z) = R(Z_h) V^2(Z_h) (p_c(x, y, \tilde{z}) - \Delta p' \tilde{z}) \quad (7)$$

where $p_c(x, y, \tilde{z})$ is periodic in $(0, \Delta\ell)$, and where $\Delta p'$ is a dimensionless pressure drop across the h -th cell. Note that by Eq. (7), the product $R(Z_h) V^2(Z_h) \Delta p'$ yields the large-scale pressure drop across the h -th cell, which must be necessarily different from zero if an average axial velocity component is to be present.

As shown in the Appendix, the small-scale fields $\mathbf{v}_c(x, y, \tilde{z})$ and $p_c(x, y, \tilde{z}) - \Delta p' \tilde{z}$ are the (h -independent) solutions of the dimensionless Navier-Stokes incompressible problem

$$\mathbf{v}_c \cdot \nabla_c \mathbf{v}_c = \frac{1}{\text{Re}} \left(\nabla_c^2 \mathbf{v}_c + (1/3) \nabla_c (\nabla_c \cdot \mathbf{v}_c) \right) - \nabla_c p'; \quad \nabla \cdot \mathbf{v}_c = 0 \quad (8)$$

defined over the generic periodic cell volume, henceforth denoted by V_c , equipped with no-slip boundary conditions onto all of the solid surfaces confining the flow, and with periodic boundary

conditions for the velocity at the opposite cross-section delimiting the unit cell. Under the assumption that the dynamic viscosity of the gas can be regarded as a constant through the entire channel, the Reynolds number

$$\text{Re} = \frac{R(Z_h) V(Z_h) \Delta\ell}{\mu} \quad (9)$$

entering Eq. (8) is independent of the cell location h since mass conservation at steady state conditions implies that (see the Appendix)

$$R(Z_k) V(Z_k) = R(Z_l) V(Z_l) \quad (10)$$

for any couple of integers $0 \leq k, l \leq N_{\text{tot}}$, where N_{tot} is the total number of cells covering the channel length. In the representation of the field variables described above, the average mass flux, say \dot{m} , through any cross-section of the generic h -th cell is thus given by

$$\dot{m} = R(Z_h) V(Z_h) = \text{const.} \quad (11)$$

from which $\text{Re} = \dot{m}\Delta\ell/\mu$. One notes that the dimensionless pressure drop $\Delta p'$ and the Reynolds number, Re cannot be fixed independently of each other in that the average axial velocity, $V(Z_h)$ is a function of the the dimensional pressure drop over a generic h cell, $R(Z_h) V^2(Z_h) \Delta p'$. This implies that the dimensionless pressure drop $\Delta p'$ across the cell is uniquely determined by the Reynolds number and the geometry of the periodic module, and thus well-defined relationship between the cell pressure drop and Reynolds number of the type

$$\Delta p' = g(\text{Re}) \quad (12)$$

must exist, where the function $g(\text{Re})$, which is proportional to the cell friction factor, only depends on the geometry of the periodic cell. Equation (12) is next used to derive the large-scale profiles of pressure, velocity and density.

3.2. Analytical prediction of the large-scale pressure profile

Consistently with the assumption of widely separated scales, when addressing the pressure, velocity and density variations along the channel, the large scale coordinate Z_h can be regarded as a continuous variable, i.e. $Z_h = Z$. Likewise, the large-scale pressure drop across the generic h -th cell is interpreted as the local gradient of the large-scale pressure at the local Z coordinate, i.e.

$$\frac{dP}{dZ} \simeq \left(\frac{\Delta P}{\Delta\ell} \right)_{Z_h} = - \frac{R(Z) V^2(Z) \Delta p'}{\Delta\ell} = - \frac{R(Z) V^2(Z) g(\text{Re})}{\Delta\ell} \quad (13)$$

Taking into account that $\dot{m} = R(Z_h) V(Z_h) = R(Z) V(Z) = \text{Re} \mu / \Delta\ell$, Eq. (13) can be re-written as

$$\frac{dP}{dZ} = - \frac{\dot{m}^2 g(\text{Re})}{\Delta\ell R(Z)} = - \frac{\mu^2 \text{Re}^2 g(\text{Re})}{\Delta\ell^3 R(Z)} \quad (14)$$

Recalling that Re is constant throughout the entire channel, Eq. (14) can be integrated by separation of variables if a relationship between the large-scale pressure and density is enforced and if the dependence of μ on the pressure P is known. In what follows, we assume that the dynamic viscosity of the fluid is independent of the pressure. The relationship $R = F(P)$ at constant temperature can be obtained by assuming that the large-scale state variables $P(Z)$ and $R(Z)$

satisfy the equation of state $f(\rho', p, T)$ of the gas (where ρ' represents the molar density of the gas), i.e. $f(R(Z)/M_w, P(Z), T) = 0$, M_w being the average molecular weight of the gas.

For instance, if $f(\rho, p, T) = 0$ is given as a virial expansion in the form

$$\frac{p}{\rho' \mathcal{R} T} = 1 + B'(T) p + C'(T) p^2 + \dots \quad (15)$$

where ρ' is the molar density of the gas and \mathcal{R} the universal gas constant, one obtains

$$\frac{R(Z)}{M_w} = \frac{1}{\mathcal{R} T} \frac{P(Z)}{1 + B'(T) P(Z) + C'(T) P^2(Z) + \dots} \quad (16)$$

which, substituted in Eq. (14) allows to derive the Z dependence of the large-scale pressure by separation of variables and quadratures. In the case of an ideal gas ($B' = C' = \dots = 0$), Eq. (14) yields

$$\frac{P^2(0)}{2} - \frac{P^2(Z)}{2} = \frac{\dot{m}^2 g(\text{Re}) \mathcal{R} T}{M_w} Z = \frac{\mu^2 \text{Re}^2 g(\text{Re})}{\Delta \ell^3} Z \quad (17)$$

If the entrance and outlet pressure are assigned, Eq. (17) can be used to compute the Re number, and thus the mass flow rate through the channel. Conversely, at fixed mass flowrate and outlet pressure, the same equation can be used to determine the inlet pressure necessary to sustain the given mass flowrate. One notes that Eq. (17) constitutes the generalization to an arbitrary spatially-periodic channel of the well-known Hagen-Poiseuille law for an ideal isothermal gas flowing through an empty straight capillary [40]. In the remainder of this article, we show how the inclusion of a much larger class of channel geometries may give rise to steady-state gas flows where the inertial term determines a Re-dependent structure of the streamline geometry. This phenomenon finds no counterpart in the Poiseuille case, where the local incompressibility assumption implies that the flow is in the Stokes regime until the critical Reynolds value marking the onset of the first hydrodynamic instability is reached.

4. Results

All of the results shown below have been obtained by solving the periodic cell and the full-scale Navier Stokes problem by the Finite Element Solver Comsol Multiphysics 6.2, using either tailored regular quadrilateral meshes (axial-symmetric geometries "(a)" and "(b)" of Fig. 2), or an unstructured tetrahedral mesh (3d helicoidal geometry, panel (c) of the same figure). For the axial-symmetric geometries, the number, N , of degrees of freedom was fixed based on the largest affordable discretization of the full-scale problem, which resulted of order $N \simeq 10^6$. The comparison between the multiscale approach-based predicted profiles and the solution of the Navier-Stokes problem in the large was carried out by using identical discretization when solving Eq. (1) and Eq. (8).

4.1. Local pressure drop

The implementation of the multiscale approach described above begins with the solution of the periodic cell problem in the interval of interest of values of the Reynolds number, from which the dimensionless pressure drop $g(\text{Re})$ can be obtained. From a practical point of view, the problem consists of fixing arbitrarily $\Delta \ell$, the fluid density and viscosity, and computing the periodic flow within the unit cell for a given interval of values of the pressure drop $\Delta p \in (0, \Delta p_{\max})$. For a given

Δp , the solution of the incompressible problem determines the average axial velocity, from which the Re value associated with Δp can be computed. Therefore, the function $g(\text{Re})$ is constructed by simply sweeping the values of Δp in the given interval and by computing Re and $\Delta p'$ *ex-post* from the average velocity obtained from the solution and from the fixed values of density and viscosity. Figure 3 (symbols) shows the results of this computation for the three geometries depicted in Fig. 2. The dashed lines in the same figure depict the scaling $g(\text{Re}) = \text{const}/\text{Re}$ pertaining to the case of a Stokes flow, where the impact of the nonlinear term in the Navier-Stokes equations is immaterial and the streamline geometry is independent of Reynolds.

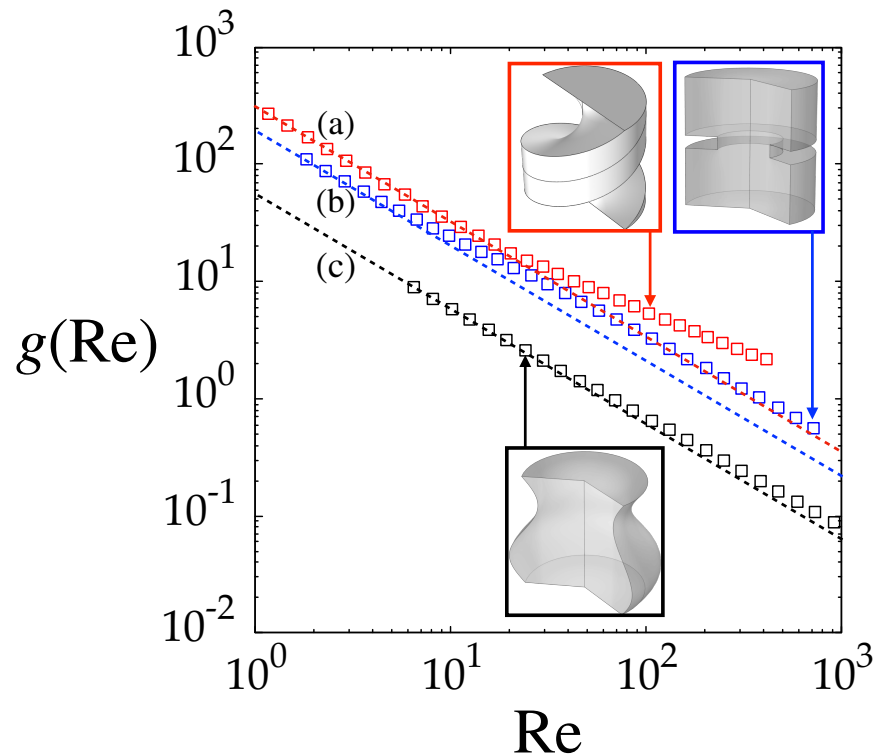


Figure 3: Dimensionless pressure drop, $\Delta p' = g(\text{Re})$ vs Re for the three case studies of Fig. 2. Black and blue symbols (c) and (b) refer to the sinusoidal and baffled axial-symmetric geometries, respectively. Red symbols (a) depict $\Delta p'$ for the 3d helicoidal geometry. Dashed lines represent the scaling $\text{const.}/\text{Re}$. Both the axial-symmetric baffled geometry and the helicoidal channel depart significantly from the $1/\text{Re}$ scaling in the range of Reynolds number considered.

The three cases considered show distinctive responses depending on the specific geometry, all characterized by positive deviations from the Re^{-1} behavior. The magnitude of the deviation increases orderly when moving from the sinusoidal channel, to the baffled and the helicoidal geometry. To unveil the origin of the large deviations from the Stokes scaling exhibited by the helicoidal channel (red symbols in the figure) let us next consider the dependence of the periodic component, \mathbf{v}_c , of the flow on Re for this specific geometry.

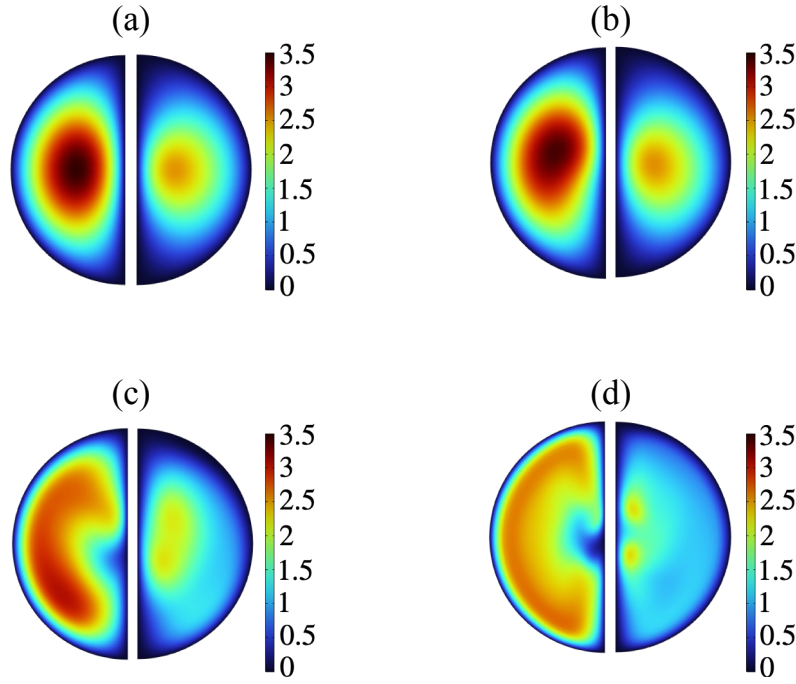


Figure 4: Transversal (left semicircle) vs axial (right semicircle) velocity magnitude for the helicoidal channel (depicted in Figure 2(c)) at increasing values of Re . Velocity values have been made dimensionless with respect to the cross-sectional average axial velocity. Panels (a), (b), (c), and (d) depict the flow structure at $Re = 1$; 10; 100; 450, respectively.

Figure 4 depicts the magnitude of the cross-sectional velocity $v_{c,\perp} = \sqrt{v_{c,x}^2 + v_{c,y}^2}$ (left semicircles) vs the axial velocity component, $v_{c,z}$ (right semicircles) at increasing values of the Reynolds number. As can be gathered from the data, the spatial distribution of the cross-sectional and axial velocity magnitude changes both qualitatively and quantitatively in such a way that the ratio $v_{c,\perp}/v_{c,z}$ is not preserved when Re varies. Because the flow streamlines are everywhere tangent to the local velocity vector, the geometry of the flow as a whole becomes Re -dependent.

4.2. Large-scale profiles

As discussed in Section 3, in the case of isothermal flow the knowledge of the local dimensionless pressure drop $g(Re)$ and the enforcement of an equation of state between the large-scale density and pressure, $R(Z)$ and $P(Z)$, respectively, allows to obtain the profile by separation of variables and integration of Eq. (14). Next, the prediction of this multiscale approach is compared and contrasted to direct the full solution of the Navier-Stokes problem in the large expressed by Eq. (1), obtained through the Finite-Element software Comsol Multiphysics (version 6.2). Owing to the large number of degrees of freedom required for solving the latter problem, only the axially-symmetric structures depicted in panel (a) and (b) of Fig. 2, which can be addressed in a two-dimensional computational

framework, have been considered. In this comparison, the volumetric behavior of the compressible fluid is assumed to obey the ideal gas law, thus yielding the pressure dependence on the large scale axial coordinate expressed by Eq. (17). Figure 5 shows the dimensionless pressure $P(Z)/P_{\text{out}}$ for the sinusoidal channel (left column) and for the baffled geometry (right column). Panels (a)-(d), (b)-(e) and (c)-(f) refer to values of the parameter $\lambda = \Delta\ell/L$ ranging from 10^{-2} to 10^{-4} , corresponding to channels embedding 10^2 to 10^4 periodic units.

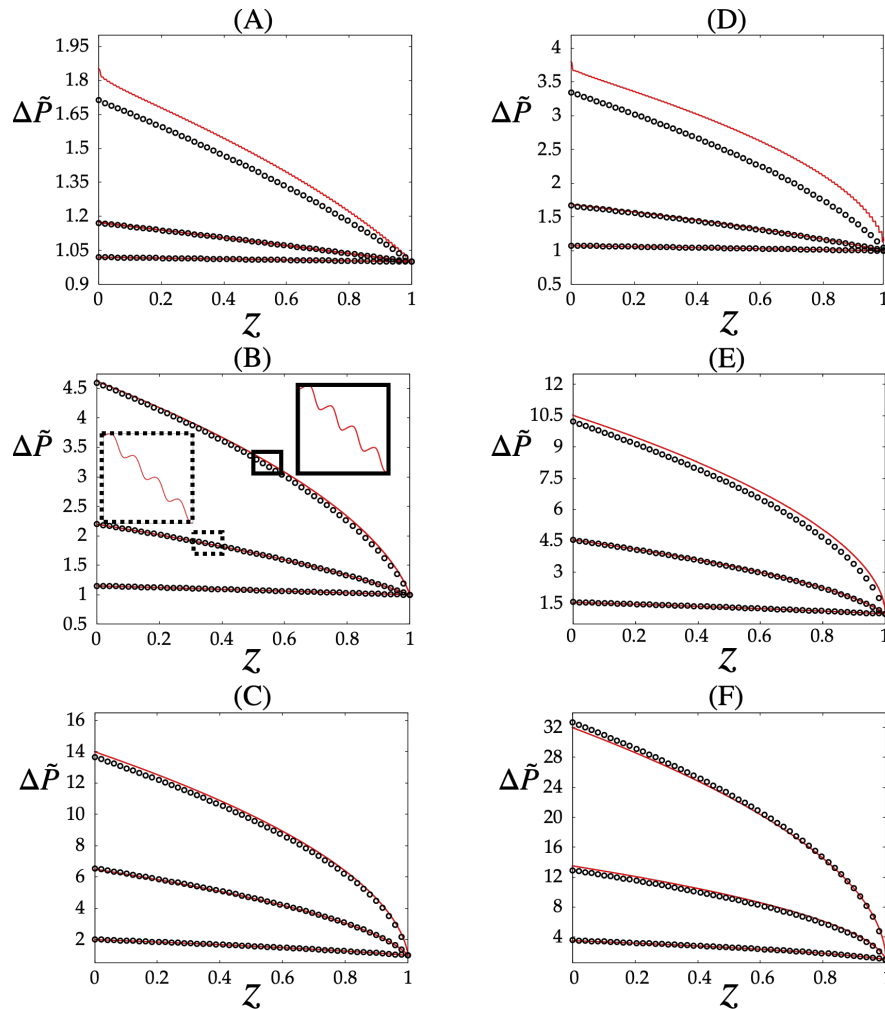


Figure 5: Comparison between the large-scale pressure as predicted by the multiscale approach (symbols) and the pressure profile at the channel axis computed by numerically solving the isothermal full-scale Navier-Stokes problem on the entire channel structure (continuous lines). The fluid is assumed to obey the ideal gas law. The arrows indicate increasing values of the Reynolds number, $Re = 10, 100, 450$. Left column: sinusoidal channel. Right column: baffled channel. Panels (a)-(d), (b)-(e) and (c)-(f) depict different levels of the scale separation parameter $\lambda = \Delta\ell/L$. (a)-(d): $\lambda = 10^{-2}$; (b)-(e): $\lambda = 10^{-3}$; (c)-(f): $\lambda = 10^{-4}$. The insets of Panel (b) show the zoomed-in pressure profile computed at the channel axis as obtained by the full-scale solution of the compressible Navier-Stokes problem of Eq. (1).

Several observations can be drawn from the data depicted:

1. The deviation from the predicted and the full-scale solution depends on the separation of scale parameter λ as well as on the Reynolds number.
2. At fixed Re value, the departure from a linear pressure scaling (constant large-scale pressure drop) depends on the specific cell geometry, as can be observed by comparing corresponding curves between left and right columns.
3. At $\lambda \leq 10^{-3}$ the multiscale approach provides an excellent estimate of the full-scale solution at all values of the Reynolds number considered, relative errors being contained within few percentage points. For instance, at $\lambda = 10^{-4}$ the relative error is order 1% even in conditions where the relative pressure variation across the channel is of order 30. the multiscale approach can either overestimate or underestimate the local pressure value.

A better insight about the validity of the local incompressibility assumption can be gained by comparing the value of the function $g(\text{Re})$ with the local value of the scaled pressure drop $\Delta p'$, as computed from the full solution of the compressible Navier-Stokes equations. Figure 6 shows the result of this comparison for the case of geometry (b) of Fig. 2. As can be observed, beyond

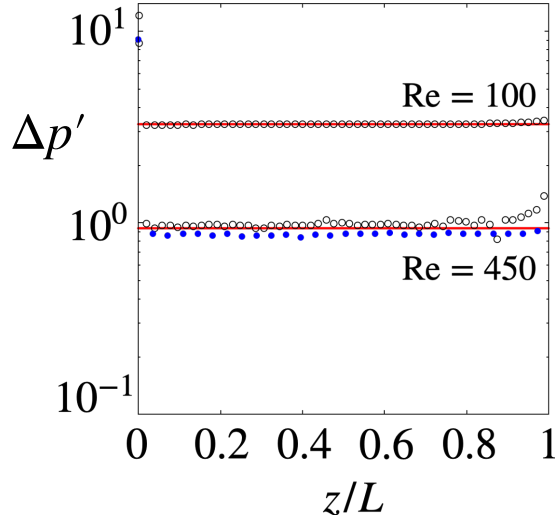


Figure 6: Comparison between the nondimensional pressure drop across a cell based on the local incompressibility assumption, $g(\text{Re})$, and the cell pressure drop as computed by the full solution of the compressible Navier-Stokes equation for the channel geometry of panel (b) of Fig. 2. Continuous (red) line: $g(\text{Re})$; empty circles: full solution at $\lambda = 2R/L = 10^{-3}$; Solid (blue) circles: full solution at $\lambda = 2R/L = 10^{-4}$.

minor fluctuations associated with the numerical discretization, the local pressure drop values are quantitatively consistent with those computed assuming locally incompressible flow throughout most of the channel axis. A consistent deviation can be observed in the region near the channel exit, where the local friction factor based on the incompressible assumption is underpredicted with respect to that computed from the full compressible Navier-Stokes problem.

Once the large-scale pressure profile has been obtained from the multiscale approach, the density $R(Z)$ can be immediately computed by the equation of state of the fluid, and the large-scale velocity $V(Z)$ can thus be obtained by mass conservation (not discussed in the interest of brevity).

4.3. Local flow structure

This much established for the large-scale profiles, we next investigate to what extent the multiscale approach can provide useful information on the small-scale structure of the flow. This issue is of fundamental importance in applications, in that the local flow structure controls both the mass and heat transport coefficients, and the very presence of the periodic geometry, possibly embedding internal obstacles and/or baffles, is often meant to obtain increased surface-to-volume ratio as well as convection-enhanced transversal transport. Figure 7 shows the side-by-side comparison of the fine structure of the velocity field within a periodic cell located halfway through the channel at different Re values as computed by the multiscale approach (left column) and the full-scale solution (right column) of the Navier-Stokes equations for a value $\lambda = 10^{-3}$ of the separation of scales parameter in both the sinusoidal and the baffled geometry. As can be observed, the fine structure

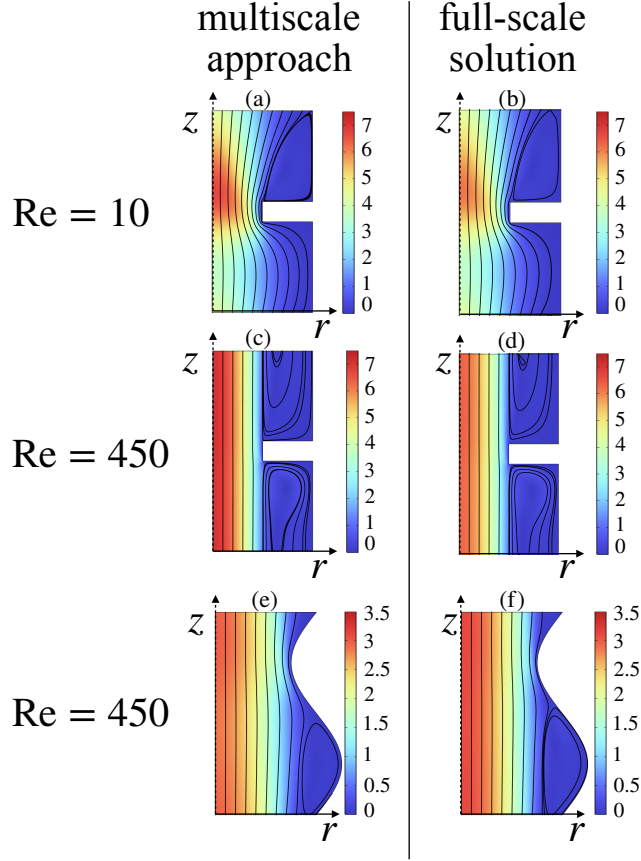


Figure 7: Comparison between the small-scale structure of the flow as computed by the multiscale approach and the full-scale solution of the Navier-Stokes compressible flow. The contour colors depict the intensity of the velocity magnitude scaled to its cell-averaged value. The continuous line represent selected flow streamlines.

of the flow is well represented by the multiscale approach both as regards the velocity intensity and the flow geometry, even at values of Re at which the non-linear term in the Navier-Stokes equation causes the streamline structure to depart significantly from that pertaining to Stokes (creeping)

flow conditions.

5. Discussion

5.1. Relevance of isothermal flows and extension to non-isothermal conditions

Among the assumptions enforced to develop the multiscale approach discussed above, the isothermal condition deserves special attention. The first issue is to determine when this assumption can be considered sensible. If one neglects the variation of specific kinetic and potential energy, the steady-state energy balance across the channel volume between the inlet and the generic cross section at \bar{Z} (see Fig. 8) dictates that

$$\mathcal{H}(\bar{Z}) - \mathcal{H}(Z=0) = \dot{Q} \quad (18)$$

where \mathcal{H} denotes the specific (mass-based) enthalpy of the gas, and where $\dot{Q}(\bar{Z})$ represents the total heat exchanged per unit mass of fluid flowing through the channel in the given channel portion. $0 \leq Z \leq \bar{Z}$.

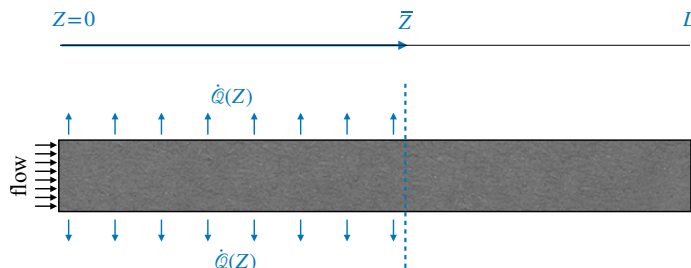


Figure 8: Schematic representation of the energy balance in a generic portion $0 \leq Z \leq \bar{Z}$ of the channel.

Let us first consider the adiabatic case, i.e. $\dot{Q} = 0$. In this case, the temperature change downstream the channel depends on the thermal and volumetric behavior of the gas through the Joule-Thomson coefficient $\alpha_{JT} = (1/c_p) (T(\partial v/\partial T)_P - v)$ where c_p is the constant-pressure specific heat and v is the specific volume. Thus the heating/cooling effect of the gas is determined by the heat capacity and the EOS of the fluid, which, in this context, is written in terms of large scale variables as $f(R(Z)/M_w, P(Z), T(Z)) = 0$. For an ideal gas, α_{JT} is identically vanishing at all pressures and temperatures, so that the adiabatic steady flow is also isothermal. Thus, in this case, the multiscale approach developed above applies with no modification, provided that the dependence of the dynamic viscosity on the pressure can be neglected. If the latter assumption holds true, then the Re number is constant, so that Eq. (8) maintains its independence of the specific position Z_h of the periodic cell. Likewise, the local pressure drop is still given by Eq. (14). If α_{JT} is different from zero, temperature changes may arise; however, even in this case, the enthalpy conservation equation enforced between the entrance ($Z = 0$) and a generic cross-section of \bar{Z} , together with the EOS of the fluid provide a system of two independent equations that allows to single out the dependence of the large-scale density on the large-scale pressure $R(Z) = F(P(Z))$. Depending on the specific form of the function F , different qualitative dependences $P(Z)$ can be found. If one were to add the effect of changes in specific kinetic energy, Eq.18 would become

$$\mathcal{H}(\bar{Z}) + \frac{R(\bar{Z}) V^2(\bar{Z})}{2} - \mathcal{H}(0) - \frac{R(0) V^2(0)}{2} = \dot{Q} \quad (19)$$

where the average velocity values at the entrance of the channel and in the generic cross-section \bar{Z} may be related through the continuity equation to the fluid density, which can be again related to local temperature and pressure values through the fluid's EOS.

In general, this argument can also be extended to the non-adiabatic case, provided that the heat-per-unit mass appearing at the right hand side of the enthalpy balance can be estimated along the channel axis. By these observations, it becomes clear that the cornerstone of the multiscale approach is the constancy of the Reynolds number along the axial coordinate, which, by mass conservation, is one-to-one with the assumption of constant dynamic viscosity of the fluid with temperature and pressure, an approximation that is not unreasonable in many practical cases. To give a quantitative example, nitrogen dynamic viscosity varies by less than 40% for $300 \leq T \leq 500$ K and $1 \leq P \leq 20$ atm.

5.2. Extension to random media

Another important issue to be addressed is the possible extension of the approach to channels embedding granular packings or random monolithic structures, which, in many applications, constitute the simplest means to obtain at one time high values of the surface-to-volume ratio and of the heat and mass transfer coefficients (the latter effect being the result of convection-enhanced transversal transport).

In this case, the concept of periodic cell must be substituted with that of a statistically representative cell, that is, a portion of length $\Delta\ell$ of the channel that is long enough as to make the values of the local pressure drop across the cell independent of the position of the cell along the channel axis. When the overall length of the channel becomes orders of magnitude larger than $\Delta\ell$, it is sensible to assume that the multiscale approach should be capable of capturing the large-scale variations of pressure, density and velocity. Clearly, given that in this case the length $\Delta\ell$ is not an unconstrained design parameter but rather results from the features of the disordered medium (be it granular or monolithic), the actual value of the separation of scale parameter must be assessed on a case by case basis.

6. Conclusions

Gas flows through periodic channel geometries exhibiting large pressure drops represent a computational challenge in that, unlike the incompressible case, the flow structure cannot be directly predicted by solving a single cell problem defined on the minimal periodic module of the structure. This makes the numerical solution of the flow troublesome, or even unattainable when complex 3d structures and relatively high values of the Reynolds number are entailed. We show that a physically sound approximation to the flow, which becomes more and more accurate as the separation of scale increases, can be obtained by a multiscale approach, where the gas velocity is split into a large-scale piecewise-constant factor, times a strictly periodic incompressible component. This allows to obtain a numerical prediction of the flow structure into two steps: -(i) solving an incompressible Navier-Stokes problem on the minimal modulus of periodicity of the structure, and -(ii) obtaining the large-scale profiles of the dependent variables by analytical integration (quadratures) of the local pressure drop across the unit cell. The method can be generalized with minimal modifications to include the non-isothermal case, provided that the dynamic viscosity of the gas can be considered constant in the range of temperatures and pressures interested. Different qualitative large-scale pressure/density/velocity profiles can be obtained depending on the structure of the equation of state of the compressible fluid and/or of the heat transfer conditions along the channel axis. The

approach is validated by comparing the prediction based on the multiscale approach with the full solution of the compressible isothermal flow of an ideal gas through different axial-symmetric periodic channel geometries. The comparison shows that when the ratio $\Delta\ell/L$ yielding the length of the periodic module to the overall channel length falls below 10^{-3} , the large scale pressure is predicted with a relative error of the order of few percent. More importantly, the local flow structure (at the scale of the periodic cell) is also accurately predicted, thus allowing the screening of a wide number of possible different cell geometries for tailored applications. The case of a cylindrical capillary embedding and helicoidal baffle is discussed in some detail as an example of 3d geometry where the enhancement of mass and heat transport coefficients can be expected due to the presence of transversal vortices, which become more and more intense with respect to the axial velocity as the Reynolds number increases. The natural extension of the approach presented in this article should be oriented towards random media, where the concept of periodic module should be substituted by that of statistically representative cell, that is, of a portion of the channel that is long enough as to make the local dimensionless pressure drop independent of its position along the channel axis.

Appendix A. Decomposition of the solution

In order to investigate the conditions under which $\mathbf{v}_c(x, y, \tilde{z})$ in eq. (5) is periodic, it is convenient to express the assumption eq. (4) on the density field $\rho(x, y, z)$ in terms of a characteristic function. Specifically, we express the density field as

$$\rho(x, y, z) = R(z) = \sum_h^N R_h \phi(z - Z_h) \quad (\text{A.1})$$

where $R_h = R(Z_h)$ is the density of the fluid in the h -th cell and $\phi(z - Z_h)$ is a distribution with compact support in the h -th cell depicted in Figure A.9.

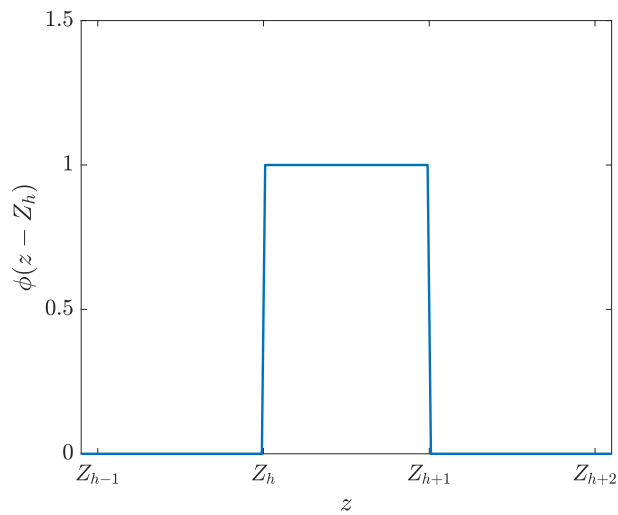


Figure A.9: Characteristic function of the generic h -th cell.

The characteristic function $\phi(z - Z_h)$ can be written as the difference of step (Heaviside) functions as

$$\phi(z - Z_h) = H(z - Z_h) - H(z - Z_{h+1}) \quad (\text{A.2})$$

Using the expression for the density eq. (A.1), the Navier-Stokes problem eq. (1) becomes

$$\begin{aligned} R(z) \mathbf{v}(x, y, z) \cdot \nabla \mathbf{v}(x, y, z) &= \mu \nabla^2 \mathbf{v}(x, y, z) + \frac{\mu}{3} \nabla (\nabla \cdot \mathbf{v}(x, y, z)) - \nabla p(x, y, z); \\ \nabla \cdot \mathbf{v}(x, y, z) &= -v_z(x, y, z) \frac{1}{R(z)} \frac{dR(z)}{dz} \end{aligned} \quad (\text{A.3})$$

where

$$\frac{dR(z)}{dz} = \sum_h^{N_{\text{tot}}} R_h (\delta(z - Z_h) - \delta(z - Z_{h+1})) \quad (\text{A.4})$$

and $\delta(z - Z_h)$ is the Dirac delta function. Considering the problem (A.3) in the h -th cell and considering $h \gg 1$ large, the boundary conditions can be expressed as

$$p(x, y, M\Delta\ell) = P_M; \quad p(x, y, N\Delta\ell) = P_N \quad (\text{A.5})$$

with vanishing velocity at the fluid-solid interfaces, where P_M is the inlet pressure on the M -th cell, P_N is the inlet pressure on the N -th cell, with $1 \leq M \ll h$ and $h \ll N \leq N_{\text{tot}} - 1$, N_{tot} being the total number of cells over the entire channel length (see Fig. A.10).

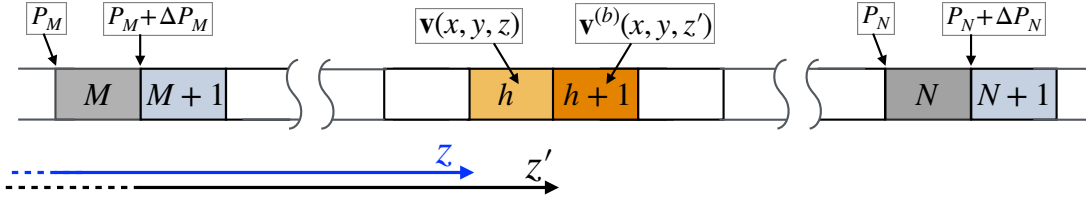


Figure A.10: Schematic representation of the reference frames z and z' used in Eqs. (A.5) through (A.9).

Without loss of generality, we can define a new Navier-Stokes solution on the $(h + 1)$ -th cell and depending on the shifted coordinate $z' = z - \Delta\ell$ such that

$$\left(\mathbf{v}^{(b)}(x, y, z'), p^{(b)}(x, y, z') \right) = \left(\mathbf{v}(x, y, z + \Delta\ell), p(x, y, z + \Delta\ell) \right) \quad (\text{A.6})$$

Furthermore, due to the periodicity of the geometry, the problem Eqs. (A.3) and (A.5) can be equivalently defined by enforcing the appropriate pressures on the adjacent $M + 1$ and $N + 1$ cells. Therefore, the equations governing the auxiliary solution $(\mathbf{v}^{(b)}(x, y, z'), p^{(b)}(x, y, z'))$ read

$$\begin{aligned} R(z') \mathbf{v}^{(b)}(x, y, z') \cdot \nabla \mathbf{v}^{(b)}(x, y, z') &= \mu \nabla^2 \mathbf{v}^{(b)}(x, y, z') + \frac{\mu}{3} \nabla (\nabla \cdot \mathbf{v}^{(b)}(x, y, z')) - \nabla p^{(b)}(x, y, z'); \\ \nabla \cdot \mathbf{v}^{(b)}(x, y, z') &= -v_z^{(b)}(x, y, z') \frac{1}{R(z')} \frac{dR(z')}{dz} \end{aligned} \quad (\text{A.7})$$

with boundary conditions

$$p^{(b)}(x, y, M\Delta\ell) = P_M + \Delta P_M; \quad p^{(b)}(x, y, N\Delta\ell) = P_N + \Delta P_N \quad (\text{A.8})$$

where $\Delta P_M = P_{M+1} - P_M$ and $\Delta P_N = P_{N+1} - P_N$. By defining the pressure field

$$\tilde{p}^{(b)}(x, y, z') = p^{(b)}(x, y, z') - \Delta P_M \quad (\text{A.9})$$

we have

$$\begin{aligned} R(z') \mathbf{v}^{(b)}(x, y, z') \cdot \nabla \mathbf{v}^{(b)}(x, y, z') &= \mu \nabla^2 \mathbf{v}^{(b)}(x, y, z') + \frac{\mu}{3} \nabla (\nabla \cdot \mathbf{v}^{(b)}(x, y, z')) - \nabla \tilde{p}^{(b)}(x, y, z'); \\ \nabla \cdot \mathbf{v}^{(b)}(x, y, z') &= -v_z^{(b)}(x, y, z') \frac{1}{R(z')} \frac{dR(z')}{dz} \end{aligned} \quad (\text{A.10})$$

with boundary conditions

$$\tilde{p}^{(b)}(x, y, M\Delta\ell) = P_M; \quad \tilde{p}^{(b)}(x, y, N\Delta\ell) = P_N + (P_{N+1} - P_{M+1}) - (P_N - P_M) \quad (\text{A.11})$$

Since $(P_{N+1} - P_{M+1})$ and $(P_N - P_M)$ are the pressure drops on an equal large number of arbitrary chosen equivalent cells, we can consider them be equal each other. Therefore,

$$\tilde{p}^{(b)}(x, y, M\Delta\ell) = P_M; \quad \tilde{p}^{(b)}(x, y, N\Delta\ell) = P_N \quad (\text{A.12})$$

Finally the density $R(z')$ is related to the pressure of the cell P_h by an Equation Of State of the fluid. At constant temperature

$$R(z') = F(P_h + \Delta P_h) \quad (\text{A.13})$$

Introducing the isothermal compressibility of the fluid

$$\beta_h = \frac{1}{R(z)} \left(\frac{\partial R(z)}{\partial P_h} \right)_T \quad (\text{A.14})$$

Therefore, for small pressure drop in the cell

$$R(z') = R(z)(1 + \beta_h \Delta P_h) \quad (\text{A.15})$$

That provides

$$\begin{aligned} R(z) (1 + \beta_h \Delta P_h) \mathbf{v}^{(b)}(x, y, z') \cdot \nabla \mathbf{v}^{(b)}(x, y, z') &= \\ \mu \nabla^2 \mathbf{v}^{(b)}(x, y, z') + \frac{\mu}{3} \nabla (\nabla \cdot \mathbf{v}^{(b)}(x, y, z')) - \nabla \tilde{p}^{(b)}(x, y, z'); \\ \nabla \cdot \mathbf{v}^{(b)}(x, y, z') &= -v_z^{(b)}(x, y, z') \frac{1}{R(z) (1 + \beta_h \Delta P_h)} \frac{dR(z)}{dz} \end{aligned} \quad (\text{A.16})$$

Comparing the original problem Eqs. (A.3) and (A.5) with the problem Eqs. (A.16) and (A.12) when $\beta_h \Delta P_h \ll 1$, we can conclude that they are the same problem with the same boundary conditions. Using the definitions Eq. (A.6) and (A.9), we obtain

$$\mathbf{v}(x, y, z + \Delta\ell) = \mathbf{v}(x, y, z) \quad (\text{A.17})$$

and

$$p(x, y, z + \Delta\ell) = p(x, y, z) - \Delta P_M \quad (\text{A.18})$$

The periodicity expressed in Eqs. (A.17) and (A.18) is fulfilled only locally. In fact, the density of the $(l + h)$ -th cell is

$$R(z') \sim R(z) \left(1 + \sum_{j=h}^l \beta_j \Delta P_j \right) \quad (\text{A.19})$$

which don't fulfil the periodicity for large values of l . In order to assess the periodicity of the solution across the entire channel, we have to decouple the thermodynamics effects due to the pressure drops along the channel from the fluid dynamics effects due to the geometry of the channel. Without loss of generality, we can define a normalized solution $(\mathbf{v}_h(x, y, \tilde{z}), p_h(x, y, \tilde{z}))$ in the h -th cell, with $\tilde{z} \in [0, \Delta l]$ such that

$$\mathbf{v}(x, y, z) = V(Z_h) \mathbf{v}_h(x, y, \tilde{z}) \quad \text{for } z \in [Z_h, Z_{h+1}] \quad (\text{A.20})$$

and

$$p(x, y, z) = P(Z_h) p_h(x, y, \tilde{z}) \quad \text{for } z \in [Z_h, Z_{h+1}] \quad (\text{A.21})$$

Using the characteristic function depicted in Figure A.9, the velocity field in the channel can be written as

$$\mathbf{v}(x, y, z) = \sum_h^{N_{\text{tot}}} V(Z_h) \mathbf{v}_h(x, y, \tilde{z}) \phi(z - Z_h) \quad (\text{A.22})$$

and

$$p(x, y, z) = \sum_h^{N_{\text{tot}}} P(Z_h) p_h(x, y, \tilde{z}) \phi(z - Z_h) \quad (\text{A.23})$$

Substituting Eq. (A.22) into the mass conservation expression of Eqs. (A.3), we have

$$\begin{aligned} R(z) \left(\sum_h^{N_{\text{tot}}} V(Z_h) \phi(z - Z_h) \nabla \cdot \mathbf{v}_h(x, y, \tilde{z}) + \sum_h^{N_{\text{tot}}} V(Z_h) \phi'(z - Z_h) v_{z,h}(x, y, \tilde{z}) \right) = \\ - \sum_h^{N_{\text{tot}}} V(Z_h) \phi(z - Z_h) v_{z,h}(x, y, \tilde{z}) \sum_h^{N_{\text{tot}}} R_h \phi'(z - Z_h) \end{aligned} \quad (\text{A.24})$$

From Eq. (A.24),

$$\nabla \cdot \mathbf{v}_h(x, y, \tilde{z}) = 0 \quad (\text{A.25})$$

if the condition

$$\begin{aligned} \sum_h^N R_h \phi(z - Z_h) \sum_h^{N_{\text{tot}}} V(Z_h) \phi'(z - Z_h) v_{z,h}(x, y, \tilde{z}) = \\ - \sum_h^{N_{\text{tot}}} V(Z_h) \phi(z - Z_h) v_{z,h}(x, y, \tilde{z}) \sum_h^{N_{\text{tot}}} R_h \phi'(z - Z_h) \end{aligned} \quad (\text{A.26})$$

is satisfied. Integrating on $z \in [Z_h, Z_{h+1}]$, the condition fulfilling Eq. (A.25) reads

$$R_h (V(Z_h) - V(Z_{h+1})) = V(Z_h) (R_{h+1} - R_h) \quad (\text{A.27})$$

Or equivalently

$$V(Z_{h+1}) = V(Z_h) \left(1 - \frac{\Delta R_h}{R_h}\right) \quad (\text{A.28})$$

with $\Delta R_h = R_{h+1} - R_h$. Therefore, by adopting a normalization of each cell following the sequence Eq. (A.28) the velocity field $\mathbf{v}_h(x, y, \tilde{z})$ is incompressible.

Using the decomposition Eq. (A.20) the expression between two adjacent cells in Eq. (A.17) becomes

$$V(Z_{h+1}) \mathbf{v}_{h+1}(x, t, \tilde{z}) = V(Z_h) \mathbf{v}_h(x, t, \tilde{z}) \quad (\text{A.29})$$

Substituting Eq. (A.28), we have

$$\mathbf{v}_{h+1}(x, t, \tilde{z})(1 - \beta_h \Delta P_h) = \mathbf{v}_h(x, t, \tilde{z}) \quad (\text{A.30})$$

which, since $\beta_h \Delta P_h \ll 1$, reads

$$\mathbf{v}_{h+1}(x, t, \tilde{z}) = \mathbf{v}_h(x, t, \tilde{z}) \quad (\text{A.31})$$

for any h (once $\beta_h \Delta P_h \ll 1$ is ensured).

Next, let us check if $\mathbf{v}_h(x, t, \tilde{z})$ the Navier-Stokes equations for the moment balance. Considering the periodicity of $\mathbf{v}_h(x, t, \tilde{z})$, we have

$$\mathbf{v}_h(x, t, \tilde{z}) \phi'(z - Z_h) = 0 \quad (\text{A.32})$$

Therefore

$$\nabla \left(\sum_h^{N_{\text{tot}}} V(Z_h) \mathbf{v}_h(x, y, \tilde{z}) \phi(z - Z_h) \right) = \sum_h^{N_{\text{tot}}} V(Z_h) \phi(z - Z_h) \nabla \mathbf{v}_h(x, y, \tilde{z}) \quad (\text{A.33})$$

Whereas, the gradient of the pressure provides

$$\begin{aligned} \nabla \left(\sum_h^{N_{\text{tot}}} P(Z_h) p_h(x, y, \tilde{z}) \phi(z - Z_h) \right) = \\ \sum_h^{N_{\text{tot}}} P(Z_h) \left(\phi(z - Z_h) \nabla p_h(x, y, \tilde{z}) + \phi'(z - Z_h) p_h(x, y, \tilde{z}) \right) \end{aligned} \quad (\text{A.34})$$

Next, we set the characteristic pressure of the cell $P(Z_h) = R_h V(Z_h)^2$ and use the scaled spatial variables $\nabla_c = \Delta \ell \nabla$ and $\zeta = \tilde{z} / \Delta \ell$. Substituting Eqs. (A.22) and (A.23) into the moment balance equation of Eqs. (A.30), and integrating over $[Z_h, Z_{h+1}]$, the equations associated to $\mathbf{v}_h(x, t, \tilde{z})$ read

$$\begin{aligned} \int_{Z_h}^{Z_{h+1}} \phi(z - Z_h) \left(\mathbf{v}_h(x, y, \tilde{z}) \cdot \nabla_c \mathbf{v}_h(x, y, \tilde{z}) - \right. \\ \left. \frac{1}{\text{Re}_h} \nabla_c^2 \mathbf{v}_h(x, y, \tilde{z}) - \frac{1}{3} \nabla_c (\nabla_c \cdot \mathbf{v}_h(x, y, \tilde{z})) + \nabla_c p_h(x, y, \tilde{z}) \right) dz = \Delta p_h; \\ \nabla \cdot \mathbf{v}_h(x, y, \tilde{z}) = 0 \end{aligned} \quad (\text{A.35})$$

where $\Delta p_h = p_h(x, y, \Delta \ell) - p_h(x, y, 0)$ and Re_h is the Reynolds number of the h -th cell, defined as

$$\text{Re}_h = \frac{R(Z_h) V(Z_h) \Delta l}{\mu} \quad (\text{A.36})$$

Eqs. (A.35) is the weak formulation of the problem

$$\begin{aligned} \mathbf{v}_h(x, y, \tilde{z}) \cdot \nabla_c \mathbf{v}_h(x, y, \tilde{z}) &= \frac{1}{\text{Re}_h} \nabla_c^2 \mathbf{v}_h(x, y, \tilde{z}) + \frac{1}{3} \nabla_c (\nabla_c \cdot \mathbf{v}_h(x, y, \tilde{z})) - \nabla_c (p_h(x, y, \tilde{z}) - \Delta p_h \zeta); \\ \nabla_c \cdot \mathbf{v}_h(x, y, \tilde{z}) &= 0 \end{aligned} \quad (\text{A.37})$$

From the Eq. (A.28)

$$R(Z_h) V(Z_h) = R(Z_h) V(Z_{h+1}) \left(1 - \frac{\Delta R_h}{R_h}\right)^{-1} \quad (\text{A.38})$$

Since $\Delta R_h/R_h < 1$, we can expand the geometric series in Eq. (A.38), obtaining

$$R(Z_h) V(Z_h) = R(Z_{h+1}) V(Z_{h+1}) (1 + O(\beta_h \Delta P_h)^2) \quad (\text{A.39})$$

where the relation Eq. (A.15) has been used.

From Eq. (A.39), it is easy to prove by recursion that, for each couple of cells j and k belonging to the channel

$$R(Z_j) V(Z_j) = R(Z_k) V(Z_k) \left(1 + O(\beta \Delta P)_{\max}^2\right) \quad (\text{A.40})$$

where $(\beta \Delta P)_{\max}$ is the maximum value of $\beta_h \Delta P_h$ over all of the h -th cells located between the cells j and k .

Finally, from Eq. (A.40), we can consider a constant Reynolds number $\text{Re} = \text{Re}_h$ across the entire channel and a periodic velocity field $\mathbf{v}_c(x, y, \tilde{z}) = \mathbf{v}_h(x, y, \tilde{z})$ solution of the equations

$$\begin{aligned} \mathbf{v}_c(x, y, \tilde{z}) \cdot \nabla_c \mathbf{v}_c(x, y, \tilde{z}) &= \frac{1}{\text{Re}} \nabla_c^2 \mathbf{v}_c(x, y, \tilde{z}) + \frac{1}{3} \nabla_c (\nabla_c \cdot \mathbf{v}_c(x, y, \tilde{z})) - \nabla_c (p_c(x, y, \tilde{z}) - \Delta p_c \zeta); \\ \nabla_c \cdot \mathbf{v}_c(x, y, \tilde{z}) &= 0 \end{aligned} \quad (\text{A.41})$$

By which

$$\mathbf{v}(x, y, z) = V(Z_h) \mathbf{v}_c(x, y, \tilde{z}) \quad \text{for } z \in [Z_h, Z_{h+1}] \quad (\text{A.42})$$

References

- [1] X. Li, Y. Huang, Z. Wu, H. Gu, X. Chen, High conversion hydrogen peroxide microchannel reactors: Design and two-phase flow instability investigation, Chemical Engineering Journal 422 (2021) 130080.
- [2] C. Li, H. Zhang, W. Liu, L. Sheng, M.-J. Cheng, B. Xu, G. Luo, Q. Lu, Efficient conversion of propane in a microchannel reactor at ambient conditions, Nature communications 15 (1) (2024) 884.

- [3] H. Feng, R. Chen, Residence time characteristics of taylor reacting flow in a microchannel reactor during long-term operation, *ACS Sustainable Chemistry & Engineering* 10 (13) (2022) 4105–4113.
- [4] J. Chen, Hydrogen production in protruded millisecond microchannel reactors by catalytically reforming methanol, *International Journal of Hydrogen Energy* 67 (2024) 225–239.
- [5] H. Bucak, F. Yilmaz, Heat transfer augmentation using periodically spherical dimple-protrusion patterned walls of twisted tape, *International Journal of Thermal Sciences* 171 (2022) 107211.
- [6] M. A. Rahman, S. M. Hasnain, R. Zairov, Assessment of improving heat exchanger thermal performance through implementation of swirling flow technology, *International Journal of Thermofluids* (2024) 100689.
- [7] V. Biagioni, C. Venditti, A. Adrover, M. Giona, S. Cerbelli, Taming taylor-aris dispersion through chaotic advection, *Journal of Chromatography A* 1673 (2022) 463110.
- [8] A. Farkya, A. S. Rana, Modeling of rarefied gas flows in streamwise periodic channels: Application of coupled constitutive relations and the method of fundamental solutions, *Engineering Analysis with Boundary Elements* 172 (2025).
- [9] V. Kosyanchuk, V. Pozhalostin, Non-stationary rarefied gas flow in a plane channel with a series of oscillating barriers, *European Journal of Mechanics, B/Fluids* 92 (2022) 90 – 99.
- [10] L. Zhu, Z. Guo, Numerical study of nonequilibrium gas flow in a microchannel with a ratchet surface, *Physical Review E* 95 (2) (2017).
- [11] A. Patronis, D. A. Lockerby, Multiscale simulation of non-isothermal microchannel gas flows, *Journal of Computational Physics* 270 (2014) 532 – 543.
- [12] R. K. Prud’Homme, T. W. Chapman, J. R. Bowen, Laminar compressible flow in a tube, *Applied scientific research* 43 (1986) 67–74.
- [13] D. C. Venerus, Laminar capillary flow of compressible viscous fluids, *Journal of Fluid Mechanics* 555 (2006) 59–80.
- [14] D. Venerus, D. Bugajsky, Compressible laminar flow in a channel, *Physics of Fluids* 22 (4) (2010).
- [15] G. Celata, M. Cumo, S. McPhail, L. Tesfagabir, G. Zummo, Experimental study on compressible flow in microtubes, *International Journal of Heat and Fluid Flow* 28 (1) (2007) 28–36.
- [16] G. Celata, M. Lorenzini, G. Morini, G. Zummo, Friction factor in micropipe gas flow under laminar, transition and turbulent flow regime, *International Journal of heat and fluid flow* 30 (5) (2009) 814–822.
- [17] X. Guo, C. Huang, A. Alexeenko, J. Sullivan, Numerical and experimental study of gas flows in 2d and 3d microchannels, *Journal of Micromechanics and Microengineering* 18 (2) (2008) 025034.

- [18] J. Bejhed, H. Nguyen, P. Åstrand, A. Eriksson, J. Köhler, Numerical modeling and verification of gas flow through a network of crossed narrow v-grooves, *Journal of Micromechanics and Microengineering* 16 (10) (2006).
- [19] S. Novopashin, P. Skovorodko, G. Sukhinin, Laminar-turbulent transition in hagen–poiseuille flow of a real gas, *Journal of Turbulence* 17 (9) (2016) 870–877.
- [20] P. Vocale, D. Rehman, G. Morini, Numerical investigation of compressibility effects on friction factor in rectangular microchannels, *International Journal of Thermal Sciences* 172 (2022) 107373.
- [21] X. Su, Y. Zhang, Y. Rao, K. Yeranee, X. Wang, Experimental and numerical study on flow and heat transfer characteristics of additively manufactured triply periodic minimal surface (tpms) heat exchangers for micro gas turbine, *Aerospace* 12 (5) (2025) 416.
- [22] Z. Cheng, X. Li, R. Xu, P. Jiang, Investigations on porous media customized by triply periodic minimal surface: Heat transfer correlations and strength performance, *International Communications in Heat and Mass Transfer* 129 (2021) 105713.
- [23] S. Jaspers, S. Schlautmann, H. Gardeniers, W. De Malsche, F. Lynen, G. Desmet, Chip-based multicapillary column with maximal interconnectivity to combine maximum efficiency and maximum loadability, *Analytical chemistry* 89 (21) (2017) 11605–11613.
- [24] D. Bragin, I. Karpilov, D. Pashchenko, Flow dynamics through cellular material based on a structure with triply periodic minimal surface, *Chemical Engineering Science* 298 (2024) 120291.
- [25] A. Meziani, S. Verloy, O. Ferroukhi, S. Roca, A. Curat, S. Tisse, V. Peulon-Agasse, H. Gardeniers, G. Desmet, P. Cardinael, Evaluation of gas chromatography columns with radially elongated pillars as second-dimension columns in comprehensive two-dimensional gas chromatography, *Analytical chemistry* 94 (41) (2022) 14126–14134.
- [26] H. Liu, J. Randon, Behavior of micro pillar array column in high pressure gas chromatography, *Journal of Chromatography A* 1656 (2021) 462551.
- [27] H. Hermann, A. Elsner, Geometric models for isotropic random porous media: a review, *Advances in Materials Science and Engineering* 2014 (1) (2014) 562874.
- [28] A. Thabet, A. G. Straatman, The development and numerical modelling of a representative elemental volume for packed sand, *Chemical Engineering Science* 187 (2018) 117–126.
- [29] D. R. Lester, G. Metcalfe, M. G. Trefry, Is chaotic advection inherent to porous media flow?, *Physical review letters* 111 (17) (2013) 174101.
- [30] H. Brenner, D. A. Edwards, *Macrotransport processes*, edited by butterworth (1993).
- [31] N. Poumaëre, B. Pier, F. Raynal, Residence time distributions for in-line chaotic mixers, *Physical Review E* 106 (1) (2022) 015107.
- [32] F. Raynal, P. Carriere, The distribution of “time of flight” in 3d stationary chaotic advection, *arXiv preprint arXiv:1412.5295* (2014).

- [33] D. R. Lester, B. Kuan, G. Metcalfe, Simultaneous optimisation of residence time, heat and mass transfer in laminar duct flows, *Chemical Engineering Science* 191 (2018) 511–524.
- [34] O. Gorodetskyi, M. F. Speetjens, P. D. Anderson, M. Giona, Analysis of the advection–diffusion mixing by the mapping method formalism in 3d open-flow devices, *AIChE Journal* 60 (1) (2014) 387–407.
- [35] C. Habchi, J.-L. Harion, S. Russeil, D. Bougeard, F. Hachem, A. Elmarakbi, Chaotic mixing by longitudinal vorticity, *Chemical Engineering Science* 104 (2013) 439–450.
- [36] R. Jilisen, P. Bloemen, M. Speetjens, Three-dimensional flow measurements in a static mixer, *AIChE journal* 59 (5) (2013) 1746–1761.
- [37] P. Gelin, D. Maes, W. De Malsche, Reducing taylor-aris dispersion by exploiting lateral convection associated with acoustic streaming, *Chemical Engineering Journal* 417 (2021) 128031.
- [38] W. De Malsche, J. Op De Beeck, S. De Bruyne, H. Gardeniers, G. Desmet, Realization of 1×106 theoretical plates in liquid chromatography using very long pillar array columns, *Analytical chemistry* 84 (3) (2012) 1214–1219.
- [39] A. J. Majda, P. R. Kramer, Simplified models for turbulent diffusion: theory, numerical modelling, and physical phenomena, *Physics reports* 314 (4-5) (1999) 237–574.
- [40] L. D. Landau, E. M. Lifshitz, *Fluid Mechanics: Volume 6, Vol. 6*, Elsevier, 1987.